

Characterization of Individual Submicron Distyrylbenzene Aggregates Using Temperature-Dependent Picosecond Fluorescence and Atomic Force Microscopy

Sang-Hyun Lim, Thomas G. Bjorklund, and Christopher J. Bardeen*

Department of Chemistry, University of Illinois, 600 S. Mathews Ave., Urbana, Illinois 61801

Received: August 3, 2003; In Final Form: December 23, 2003

The time-resolved fluorescence of individual distyrylbenzene aggregates is studied in order to determine the effects of aggregate morphology on the emission properties. Using a confocal microscope and a photon-counting streak camera, we measure the full time and wavelength dependence of the fluorescence from individual submicron aggregates at the temperatures 290, 100, and 4 K. The morphology of these aggregates is characterized separately using tapping-mode atomic force microscopy. All aggregates show temperature-dependent fluorescence decays and spectral shifting, most likely due to activated energy transfer to lower energy sites which correspond to spectrally distinct species. We find significant aggregate-to-aggregate variations in the fluorescence spectra and decays, but the amount of variation depends on preparation conditions: solvent-annealed aggregates have a more uniform appearance and less variation in their spectral properties. To analyze the data, we model the dynamics in terms of two coupled states, which correspond to the intrinsic exciton in solid DSB and a lower energy defect. Even this simple model requires additional assumptions, but it allows us to extract spectra corresponding to both species, and generate histograms of the two different decay rates. Variations in the decay rates are ascribed to variations in the concentration of quenching defects between individual aggregates.

Introduction

Organic semiconductors are a subject of intense interest due to their potential applications ranging from light-emitting diodes to solar cells to thin-film transistors.^{1,2} One group of organic semiconductors that has been extensively studied are the phenylene-vinylene (PV) polymers, like poly(*p*-phenylene-vinylene) (PPV) and poly[2-methoxy-5-(2'-ethylhexyloxy)-1,4-phenylene-vinylene] (MEH-PPV). These polymers, however, are very complicated and not well-characterized at the molecular level, due to their polydispersity and unknown levels of chemical impurities. To better understand the molecular level interactions in these polymers, for example the extent of electronic wave function delocalization, model oligomer systems have been studied as well.^{3,4} Advantages of studying the oligomers include the ability to obtain high purity, single component samples and the ability to study the unaggregated molecule in dilute solution. Oelkrug and co-workers have looked at the properties of PV oligomers, both isolated and aggregated, in hopes of better understanding how the intermolecular interactions affect the properties of neat polymer films.^{5–8} Theoretical analysis of the aggregate spectra by Spano et al. has provided good evidence that the spectroscopy is dominated by excitonic states arising from the herringbone lattice of strongly coupled molecules, along with assorted defects.^{9–11} In fact, from an analysis of the vibronic line shape of the “free exciton” emission in such aggregates, it should be possible to estimate the exciton coherence length.¹²

It is clear that the study of oligomeric PV aggregates can help improve our understanding of electronically coupled organic aggregates and thus the properties of conjugated polymers such as PPV. However, although the spectroscopic

characterization of dilute oligomers is straightforward, the aggregate properties are very sensitive to preparation conditions, and large sample-to-sample variations in basic properties such as the fluorescence spectrum and lifetime can be observed. It is therefore interesting to study the connection between the spectroscopy and morphology in these systems, with the goal of understanding how variations in PV aggregate structure can give rise to different optical properties. In this work, we use microscopy to study the properties of individual submicron-scale aggregates, in the hopes that the spectroscopy of individual aggregates will provide insight into the behavior of thin films. The specific oligomer studied in this work is distyrylbenzene (DSB), which corresponds to a segment of PPV extending over three phenyl rings, as shown in Figure 1. This is the shortest PV segment that has good light-emitting properties: unlike stilbene, its quantum yield is close to unity and its isomerization quantum yield is negligible. Although the polycrystalline morphology of phenylene-vinylene oligomer thin films can vary considerably,^{13–15} atomic force microscopy of DSB thin films shows that evaporated films consist of relatively large, $\sim 1 \mu\text{m}$ domains.¹⁶ As in Oelkrug's work,⁵ we find that the optical spectroscopy of DSB aggregates is very sample dependent, most likely due to various levels of different defect states which spectrally overlap. We find that micron-size DSB aggregates can show large variations in both fluorescence spectrum and lifetime from aggregate to aggregate. Even within a single aggregate, there are several types of emitting species which lead to nonexponential fluorescence decays and spectral shifting. Aggregates annealed under solvent vapor show more reproducible behavior from aggregate to aggregate, although there is still some variation. In the annealed sample, we use a multiwavelength biexponential fitting procedure to decompose the fluorescence decay for individual aggregates into two types of emitting species. We interpret these two species in terms of

* To whom correspondence should be addressed.

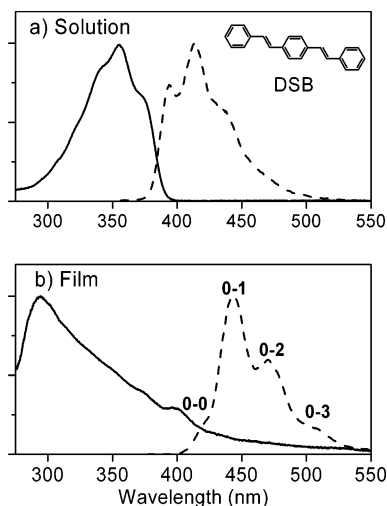


Figure 1. Absorption (solid curve) and emission (dashed curve) spectra of DSB (a) dissolved in THF and (b) evaporated film. The emission peaks are labeled 0–0, 0–1, 0–2, and 0–3 as described in the text. Also shown is the structure of a DSB molecule.

two states, with the lower energy “defect” state populated both by direct excitation and by thermally activated transfer from the higher energy “free exciton” state. The transfer rate varies between different aggregates in the sample, most likely due to the presence of different concentrations of defects within those aggregates. The fact that even on the micron scale there is heterogeneity in these aggregates attests to the strong intermolecular coupling in solid DSB and the nonequilibrium preparation conditions.

Experimental Section

To measure both the photodynamics and morphology of individual molecular aggregates, we use confocal fluorescence microscopy in conjunction with streak camera detection. These experiments are similar in spirit to earlier work by Barbara^{17–20} and others,^{21–24} who used near-field scanning optical microscopy to characterize the morphology and spectroscopy of single molecular aggregates. The present approach permits the study of such aggregates under vacuum and at variable temperatures. The experiment consists of three main phases: synthesis and deposition of the aggregates, measurement of the time-resolved fluorescence, and finally characterization using tapping mode atomic force microscopy (AFM). These three phases are described in detail below.

To make the aggregates, a 1×10^{-3} M solution of DSB in tetrahydrofuran (THF) or dimethylformamide (DMF) is put in a nebulizer (Compair model NE-C18, Omron), which makes small droplets ($0.5 \mu\text{m} - 5 \mu\text{m}$ in diameter) which are deposited onto cleaned microscope coverslip substrates (see below). The combination of small droplet size and the distance of the substrate from the nebulizer nozzle results in the formation of small aggregates, spaced by several microns from each other on average. The aggregates range in size from 500 nm to several microns. The initial deposition results in aggregates with high surface roughness and widely varying shapes. These aggregates can be annealed by leaving them in a sealed container with the original solvent. After a period of 2 h or more, the aggregates are observed to form more uniform shapes with smoother surfaces. Comparison of fluorescence images before and after the solvent annealing shows that the original aggregates completely redissolve and form new aggregates during this procedure.

Since we wish to study the correlation between morphology and photodynamics, we need to be able to locate specific aggregates in two different experimental setups. This is done by patterning the substrates using amplified femtosecond laser pulses. Coverslips are used because they are optically clear and can withstand the pressure necessary for achieving good thermal contact with the copper surface of the cryostat coldfinger. The coverslips are put on a XY translational stage which is scanned by a personal computer to trace grid patterns ($50 \mu\text{m}$ by $50 \mu\text{m}$ squares) using laser damage. These substrates are then cleaned using methods shown to leave very flat surfaces.²⁵ The patterned substrates are first treated for 20 min in a mixture of 1:1:5 (v/v/v) 25% ammonia, 30% hydrogen peroxide, and deionized water heated to between 70 and 80 °C with stirring. The substrates are then transferred to another solution of 1:1:5 (v/v/v) concentrated hydrochloric acid, 30% hydrogen peroxide, and water. This solution is also heated to between 70 and 80 °C with stirring. After 20 min in the second solution, the substrates are transferred to a beaker with 20 mL of 30% hydrogen peroxide. The peroxide is poured out, and another 20 mL of peroxide is added and then stirred by hand. The peroxide is poured out, and 20 mL of Optima methanol is added and stirred by hand. The substrates are transferred to another beaker containing 20 mL of Optima dichloromethane. The dichloromethane is poured out, and 20 mL of diethyl ether is added and stirred by hand. The substrates are then removed and placed in a desiccator until needed. The cleaned glass coverslips have a surface roughness on the order of 2 nm, which is suitable for use as an AFM substrate. The aggregates are deposited on the opposite side of the laser etched pattern to avoid confusing damaged areas with deposited aggregates.

Once a sample is made, it is transferred into the microscope cryostat (ST-500, Janis). The DSB aggregates must be studied under vacuum in the cryostat to avoid photooxidation and to allow the sample temperature to be varied. Excitation pulses are obtained using a femtosecond Ti:sapphire oscillator operating at 750 nm. The oscillator pulse repetition rate of 91 MHz can lead to local heating in the sample, which results in a faster decay of fluorescence and broadening of the fluorescence spectrum. To eliminate this problem, the repetition rate is reduced to 500 kHz using a pulse-picker based on a Pockels Cell (Conoptics 350–160). After reducing the repetition rate to 500 kHz, the 750 nm pulses are compressed with a prism pair and frequency doubled in a 0.4 mm BBO crystal. The resulting 375 nm pulses are filtered with a short wave pass filter (500 nm cut off frequency) and delivered to the microscope. To minimize the spectral distortion, a fused silica optical wedge is used instead of a dichroic mirror to reflect the excitation pulses and transmit the fluorescence to the detectors. The excitation spot is scanned using a mirror whose orientation is controlled with two linear actuators (T-LA28, Zaber Technologies) linked to a personal computer. The laser is linearly polarized before the microscope, while there is no polarization selection in the detection optics. In general, the amount of fluorescence depended on the alignment of the aggregate relative to the laser polarization: rotating the laser polarization 90° usually resulted in a change in fluorescence intensity of a factor of 2–3. This provides an indication that the aggregates are anisotropic and at least partially retain their crystalline orientation. We did not systematically study the dependence of the fluorescence spectrum on either excitation or detection polarization. A 0.6 N.A. long working distance objective (Olympus) is used to focus the excitation pulses and collect the fluorescence signal. For confocal microscope imaging, the fluorescence is focused into

a pinhole with a 10 cm lenses and detected with a photon counting photomultiplier tube (H7421, Hamamatsu). A GG 420 filter (Andover Corp.) is used to remove scattered excitation light. By scanning the excitation spot over the correct grid square on the patterned substrate, a fluorescence image is obtained, mapping out the locations of the individual aggregates. After deciding upon a specific aggregate to be studied, the excitation spot is moved to that aggregate and the fluorescence is directed to the streak camera (Hamamatsu C4334) by switching a flip-up mirror.

After the streak camera experiments, the sample is removed from the cryostat and imaged using tapping-mode atomic force microscopy (Dimension 3100, Digital Instruments). The aggregates are identified by comparing the AFM image in a particular grid with the image obtained from the fluorescence microscope. We have found that contact mode AFM causes irreversible damage to the aggregates, often fragmenting them, but that tapping mode is gentle enough to leave them intact. Even after imaging the aggregates for several hours under air, we can place them back in the cryostat and obtain fluorescence data that matches previous experiments on the same aggregates.

Results

Figure 1a shows the absorption and fluorescence of monomeric DSB in dilute tetrahydrofuran solution. The absorption peaks at 350 nm and the emission line shape is close to a mirror image of the absorption, as expected for a molecule that does not undergo large distortions in its excited state. The structure in both spectra is due to vibrational modes with frequencies ranging from 1100 to 1400 cm^{-1} , which most likely correspond to double bond stretches or phenyl breathing modes in the molecule. This vibrational structure is commonly seen in the PV family of molecules.^{26,27} When DSB is deposited onto a glass substrate, using a variety of methods ranging from solution evaporation, vacuum sublimation, or deposition of reprecipitated aggregates, the resulting absorption is markedly different from that observed in solution, as can be seen in Figure 1b. The absorption is strongly broadened, with the main peak at 300 nm and a long tail extending past 400 nm. This absorption has the basic characteristics of an H-aggregate, with a strongly blue-shifted absorption peak due to excitonic splitting of the molecular excited states.²⁸ Recent theoretical calculations have estimated this splitting to be on the order of 1 eV,¹⁰ due to very strong Coulombic interactions between the DSB molecules residing in the DSB crystal's herringbone lattice. The emission line shape is more difficult to understand, but is thought to originate from both excitons and various types of defects in the aggregates. The main features of the emission are the shoulder at 420 nm, and the progression with peaks at 440 nm, 470 nm, and a broader peak extending past 500 nm. In analogy with the molecular fluorescence spectra, we label these peaks as vibronic transitions with the highest energy 420 nm peak corresponding to the 0–0 transition, the 440 nm peak denoted by 0–1, and so on. We have found considerable variation in the emission line shape depending on the preparation conditions of these thin films. Vacuum deposited films, solution deposited films, and even colloidal suspensions in water can give noticeably different fluorescence spectra at room temperature. This sensitivity of the steady-state spectral properties to preparation conditions has been observed previously in DSB aggregates reprecipitated in water,⁵ as well as in neat films of PV polymers such as PPV²⁹ and MEH–PPV,^{30,31} where aggregation is also expected to play an important role in the spectroscopy. To investigate the dependence of the spectroscopy on the morphol-

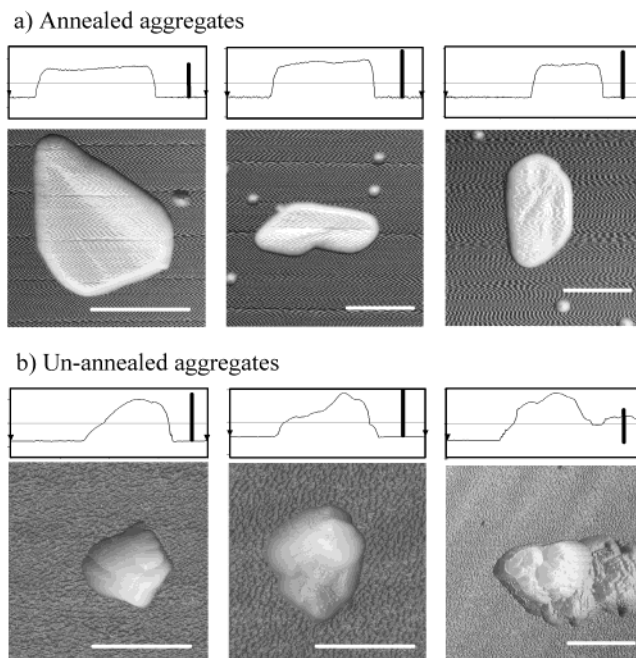


Figure 2. AFM images and profiles of typical (a) annealed and (b) unannealed DSB aggregates. Vertical scale bars = 100 nm, horizontal scale bars = 1 μm .

ogy of aggregation, we next examine individual aggregates of DSB, deposited from solution.

In Figure 2, we show tapping-mode AFM images of three representative aggregates from two different types of samples: as-deposited using DMF microdroplets and solvent-annealed aggregates after exposure to 12 h of saturated DMF vapor at room temperature. The solution deposited DSB aggregates shows considerable variation in the shapes of the aggregates, and similar levels of heterogeneity have been observed in solution-deposited conjugated oligomer thin films.^{15,32} As observed previously for inorganic microcrystals, the solvent-annealed aggregates are smoother and more uniform in appearance than the unannealed aggregates.³³ Their flat tops and smooth sides contrast with the irregular features seen in the unannealed aggregates. In both samples, the aggregates range in size from a few hundred nanometers in diameter to over a micron, but they are relatively platelike in that most are less than 100 nm in height. In the data below where we analyze variations between individual aggregates within a sample, we use a single sample of 10 aggregates. We are limited to this number because of the time-intensive nature of the experiments and because we want to be sure that there is no difference in sample preparation or experimental conditions when we look at aggregate-to-aggregate variations. Experiments on other sample sets on different days give results that are identical to within the statistical error.

We first compare the fluorescence spectra and lifetimes of the annealed and unannealed samples. In Figure 3, we show representative early (0–0.5 ns) and late (3–4 ns) time spectra for both types of aggregates at three different temperatures: 290, 100, and 4 K. Two main features of the data are immediately apparent. First, in all of the samples, the fluorescence spectrum not only shifts but also changes shape over the course of nanoseconds. The only exception is the unannealed aggregates at 4 K, where the spectrum shifts by ~ 5 nm but does not change appreciably. All of the other samples not only shift, with the low energy side of the spectrum becoming enhanced relative to the high energy side. This change is especially dramatic in

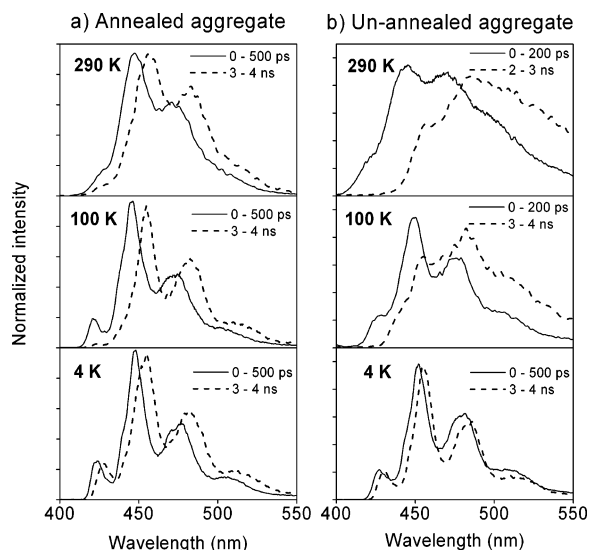


Figure 3. Time-resolved emission spectra for (a) annealed and (b) un-annealed DSB aggregates at 290, 100, and 4 K. Note that for the un-annealed aggregate at 290 K, the emission decays so quickly that we choose a different time window.

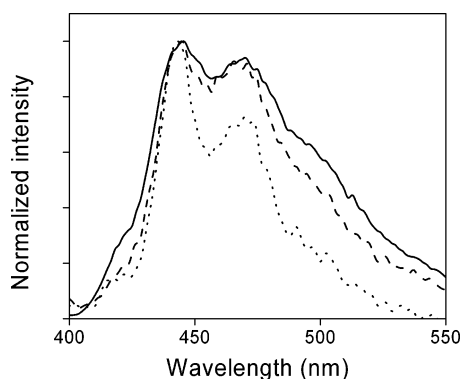


Figure 4. Early-time (0–200 ps) normalized fluorescence spectra for the three un-annealed aggregates shown in Figure 2b at 290 K.

the unannealed aggregates at 100 and 290 K, where the spectral shape after 4 ns bears little resemblance to the early-time spectrum. For the annealed aggregates, the shift is always accompanied by an enhancement of the 0–2 and 0–3 peaks relative to the 0–0 and 0–1 peaks. This enhancement is not as temperature-dependent as in the unannealed aggregates, but persists even at 4 K.

Differences between aggregates exist even within a given sample preparation, although they are not as dramatic as those between the different sample types. Figure 4 shows the variation in early-time (0–0.2 ns) spectra for several unannealed aggregates at 290 K, where the intra-sample variation is most pronounced. Even here, the actual difference between the three spectra is mainly in the broadening of the peaks and not in the actual position of the lines. As the temperature is lowered, the spectral differences between individual aggregates disappear. At 4 K, there is essentially no variation between aggregates in a given sample at either short or long times. Of course, there are still differences between the annealed and unannealed samples, as can be seen from Figure 3.

The other aspect in which the annealed and unannealed aggregates differ is in the amount of variation in their fluorescence lifetimes. In general, the different spectral components decay at different rates, and this leads to nonexponential decay dynamics. Before analyzing these multicomponent decays in detail, we illustrate the aggregate-to-aggregate variation in

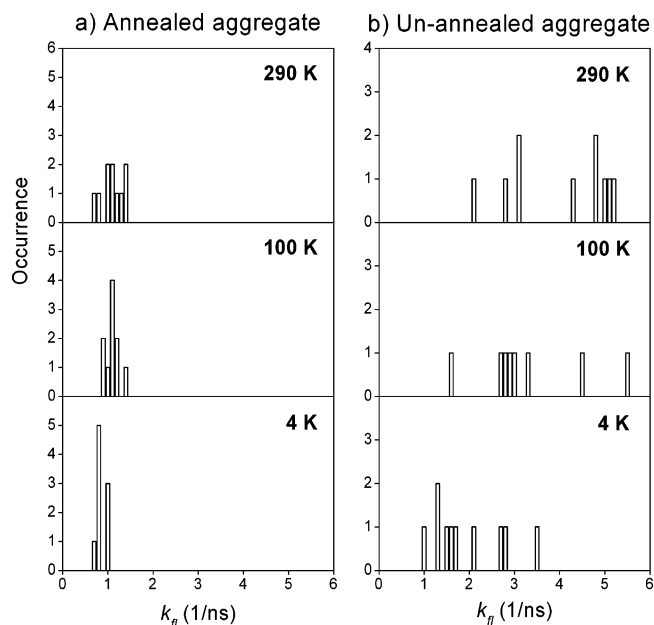


Figure 5. Histograms of averaged emission decay rates, as defined in eq 2, for (a) annealed and (b) un-annealed aggregates at 290, 100, and 4 K.

the overall decay of the integrated fluorescence by defining an averaged fluorescence decay rate for each aggregate. The normalized fluorescence decays, integrated over all wavelengths, can be fit using a biexponential decay of the form

$$F_{\text{tot}}(t) = Ae^{-k_A t} + Be^{-k_B t} \quad (1)$$

where the average fluorescence decay rate is defined as

$$\frac{1}{\langle k_f \rangle} = \frac{A}{k_A} + \frac{B}{k_B} \quad (2)$$

Figure 5 shows histograms of the average fluorescence lifetimes for both annealed and unannealed samples, each consisting of 10 aggregates, at 290, 100, and 4 K. Although the annealed samples' decay rates show little intra-sample variation and steadily decrease as the temperature is lowered, the unannealed rates vary widely at all temperatures. Even at 4 K, where all of the aggregate spectra are identical, their averaged decay rates vary by a factor of 3. This variation in the decay rates leads to different weightings of the redshifted, long-time component relative to the early-time emission, especially at room temperature, and thus leads to variations in the integrated fluorescence spectrum as well.

Our analysis so far has centered on the differences between annealed and unannealed aggregates, with the conclusion that aggregate-to-aggregate variations can be suppressed by an extended period of solvent annealing. The shifting and reshaping of the fluorescence spectrum suggests the presence of multiple types of emitting species within single aggregates, both in annealed and unannealed samples. These multiple emitting species probably consist of a mixture of intrinsic or “free” exciton emission and emission from multiple types of structural defects. The decomposition of the fluorescence spectrum into these components is desirable for several reasons. First, we wish to identify the intrinsic exciton spectrum in these aggregates and compare it with that predicted by theoretical models based on solving the exciton–phonon Hamiltonian. Recent work has shown how the vibronic structure and in particular the height of the 0–0 peak relative to the replica peaks can be a very

sensitive indicator of exciton coherence length.¹² Second, the spectra of the defects can also be compared with theoretical models for structures such as dislocations and slip boundaries in order to determine the identity of the defects.¹¹ Once such defects have been identified, a chemical strategy can be devised to eliminate them.

As a first attempt to accomplish such a decomposition, we take the annealed spectra at 100 K as our model system. We choose these data because the decomposition results provide the clearest illustration of how the two different emitting species with different lifetimes can explain our time- and wavelength-resolved fluorescence data. At room temperature, the broadened spectra are less distinct, whereas at 4 K, the emission is dominated by a single emissive state, as shown in Figure 3. We use the simple model outlined in Figure 6 to analyze these data. The assumption that only two distinct species, a free exciton and a defect, contribute to the fluorescence is probably an oversimplification but is necessary in order to do a multi-parameter fit to the experimental data. The evolution of the populations in states 1 and 2 are governed by the coupled rate equations

$$\frac{dN_1}{dt} = -(k_1 + \Gamma)N_1 \quad (3a)$$

$$\frac{dN_2}{dt} = +\Gamma N_1 - k_2 N_2 \quad (3b)$$

where k_1 is the relaxation rate from state 1 to the ground state, k_2 is the relaxation rate from state 2 to the ground state, Γ is the trapping rate from state 1 to state 2, and we assume there is no back transfer from level 2. These equations are easily solved to give

$$N_1(t) = N_1^0 e^{-(k_1 + \Gamma)t} \quad (4a)$$

$$N_2(t) = \left(N_2^0 - \frac{N_1^0 \Gamma}{k_2 - (k_1 + \Gamma)} \right) e^{-k_2 t} + \frac{\Gamma N_1^0}{k_2 - k_1 - \Gamma} e^{-(k_1 + \Gamma)t} \quad (4b)$$

where N_1^0 and N_2^0 are the initial populations in states 1 and 2 created by the excitation pulse. If level 1 gives rise to an emission spectrum with a line shape described by $F_1(\lambda)$ and level 2 gives rise to $F_2(\lambda)$, then the total time-dependent fluorescence is

$$\begin{aligned} F_{\text{tot}}(\lambda, t) &= N_1(t)F_1(\lambda) + N_2(t)F_2(\lambda) \\ &= N_1^0 \left(F_1(\lambda) + \frac{\Gamma F_2(\lambda)}{k_2 - k_1 - \Gamma} \right) e^{-(k_1 + \Gamma)t} + \\ &\quad F_2(\lambda) \left(N_2^0 - \frac{N_1^0 \Gamma}{k_2 - k_1 - \Gamma} \right) e^{-k_2 t} \end{aligned} \quad (5)$$

Equation 5 predicts an experimental signal of the form

$$F_{\text{tot}}(\lambda, t) = A_1(\lambda) e^{-(k_1 + \Gamma)t} + A_2(\lambda) e^{-k_2 t} \quad (6)$$

with $A_2(\lambda)$ being directly proportional to the emission spectrum of state 2, $F_2(\lambda)$. At each wavelength, λ the fluorescence decay is biexponential, and the two decay rates, $k_1 + \Gamma$ and k_2 , are the same for all λ 's. The prefactors A_1 and A_2 for these two exponential terms depend on λ , however, and can even be negative if $\Gamma \neq 0$. Although it is straightforward to determine $F_2(\lambda)$ from $A_2(\lambda)$, to extract $F_1(\lambda)$, we need to know both the

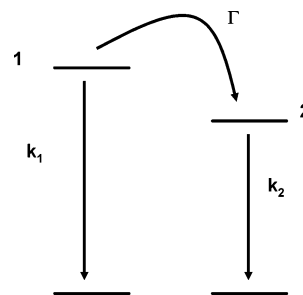


Figure 6. Level diagram for analysis of the experimental data. Level 1 corresponds to the intrinsic exciton, whereas level 2 represents lower energy defect states.

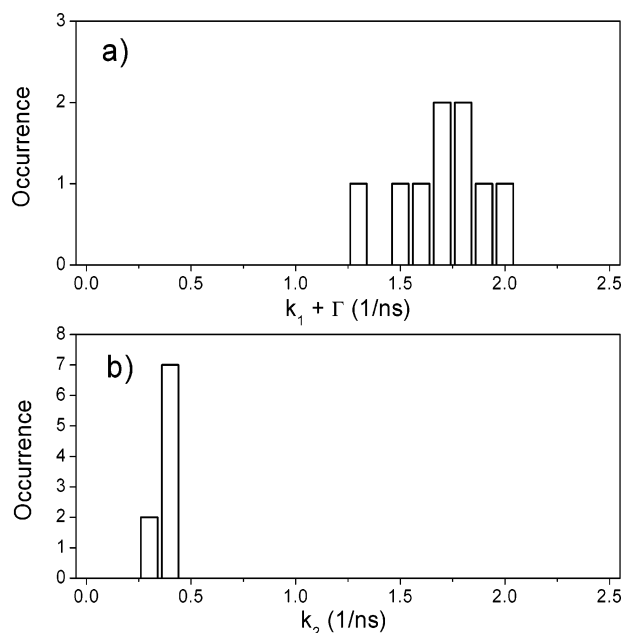


Figure 7. Histograms of the decay rate at 100 K for (a) level 1, $k_1 + \Gamma$ and (b) level 2, k_2 .

ratio N_1^0/N_2^0 and Γ . The decay rates $k_1 + \Gamma$ and k_2 can be extracted from the fit, but the most we can say is that $\Gamma \neq 0$ if we find that $A_1(\lambda) < 0$ at some wavelengths. There are not enough constraints in the model to extract the individual components of k_1 and Γ , and also $F_1(\lambda)$.

To analyze the data in terms of the above model, the full time and wavelength-dependent fluorescence data is fit using a biexponential function, where the decay constants $k_1 + \Gamma$ and k_2 are varied to obtain the best global fit to the data. The amplitudes $A_1(\lambda)$ and $A_2(\lambda)$ are obtained as outputs from the linear regression at each wavelength. We analyze all 10 of the annealed aggregates in the manner described above and determine two exponential decay rates for each one. Figure 7a plots a histogram of the values obtained for $k_1 + \Gamma$, and Figure 7b shows the values for k_2 . The combined rate $k_1 + \Gamma$ varies by 20% or more, whereas Figure 7b shows that k_2 hardly varies at all in the same sample. Data on different samples taken on different days show distributions which are not statistically different from those in Figure 7, parts a and b. It is the variations in $k_1 + \Gamma$ that lead to the small variations in the averaged fluorescence lifetimes in Figure 5. The most likely reason for this variation is a changing value of Γ , the rate of trapping to state 2. The physical origin of this variation could be that the different aggregates have different concentrations of trap sites. A simple estimate of the trapping rate involves the product of an intrinsic rate, e.g., the diffusion of the initially created exciton, and the concentration of traps it encounters, i.e., $\Gamma = k_{\text{trap}}[\text{trap}]$.

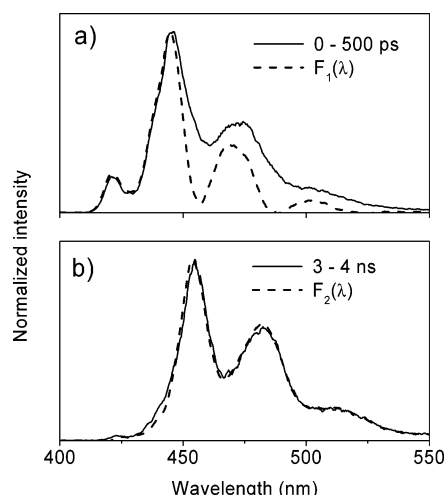


Figure 8. (a) Comparison of 0–500 ps experimental spectrum at 100 K and the fast component $F_1(\lambda)$ obtained from data analysis based on eq 5. (b) Comparison of 3–4 ns experimental spectrum at 100 K and the slow component $F_2(\lambda)$.

This would naturally lead to variations in Γ and thus the total rate $k_1 + \Gamma$. As is the case for the unannealed aggregates, the most important variation is not in the spectra but in the rates.

Extracting the individual spectra $F_1(\lambda)$ and $F_2(\lambda)$ is more difficult. There are two simple cases. If we assume that state 2 is not populated at all by the excitation, i.e., $N_2^0 = 0$, then the early time spectrum is exactly $F_1(\lambda)$, i.e., $F_{\text{tot}}(\lambda, 0) = F_1(\lambda)$. If we assume that there is no transfer between the states, i.e., $\Gamma = 0$, then $A_1(\lambda)$ is directly proportional to $F_1(\lambda)$. Neither assumption is well-justified in our experiments. To illustrate the modeling, we take an intermediate case and assume $N_1^0 = N_2^0$. To determine Γ , we assume that $\Gamma = 0$ at 4 K and assume k_1 is just the short time component measured at 4 K. The $F_1(\lambda)$ and $F_2(\lambda)$ spectra obtained using these approximations and eq 5 are compared to the experimental spectra at early (0–0.5 ns) and later (3–4 ns) delays in Figure 8. The spectra obtained from the fits resemble the time windowed spectra, but there are some differences in the relative peak heights, especially for the 0–2 and 0–3 peaks in the early-time spectra. These differences are due to the fact that even at the earliest delays we can measure with good signal-to-noise both the species contribute to the fluorescence. Only after the short-lived state 1 decays sufficiently does the experimental spectrum reflect a single species, namely the longer-lived state 2. Fits to all of the annealed aggregates result in similar sets of spectra. We emphasize that the spectra in Figure 8 are not necessarily the true exciton and defect spectra of DSB: they serve mainly to illustrate that the procedure gives reasonable results.

Discussion and Conclusions

Our experiments on isolated DSB aggregates are designed to help clarify the origins of the sensitivity of the thin film spectroscopy to sample preparation conditions. One possible explanation for the variance we see in the spectroscopy of the aggregates is that it is an artifact due to different amounts of self-absorption in the aggregates. We found no correlation between aggregate thickness and fluorescence decay rates, however, as predicted by models of self-absorption effects.³⁴ The small size of these aggregates, along with their weak absorption near 400 nm, means that the strong self-absorption and waveguiding effects seen in previous studies of individual J-aggregate crystals³⁵ should be much weaker for DSB. We have found that in dense films of evaporated DSB at room temper-

ature, there are clear signatures of self-absorption and radiative energy transfer from the high energy side of the emission to the low energy side. These more dramatic effects are well-fit using simple expressions for self-absorption and re-emission.³⁴ The main signature of this phenomenon is an overall increase in the red edge of the emission that mirrors the decay of the blue edge. This growing-in disappears when very thin (<0.2 OD at 400 nm) films or single aggregates are examined. If one is not careful to test for self-absorption by varying the film thickness or by doing experiments on individual aggregates, such effects can be mistaken for energy transfer dynamics.

The most likely explanation for the differences between aggregates is that they have different concentrations and distributions of trapping sites. In this case, the spectral shifting and lifetime shortening reflects the defect density. This interpretation of the spectral dynamics parallels that for films of phenylene vinylene oligomers^{5,36} and for isolated J-aggregate crystals,³⁵ where similar shifting and shape changes have been ascribed to energy migration to trapping sites. The differences in trapping we see between different unannealed aggregates from the same sample are most likely due to slightly different formation conditions. Even though DMF has a low vapor pressure, the small ($<5 \mu\text{m}$) droplets used to make the isolated aggregates have a very high surface-to-volume ratio and evaporate very quickly. This nonequilibrium process would be expected to lead to highly disordered structures which are frozen in place, as observed in spin-coated polymer films which form under similar fast-drying conditions.³⁷ The AFM measurements confirm this enhanced structural disorder in the deposited aggregates. This frozen disorder then leads to more or less variation in site energies, as deduced from the different amounts of broadening seen in Figure 4. Even more pronounced is the variation in fluorescence lifetimes for those species. This is seen most dramatically at 4 K, where the time-dependent spectra are almost identical for all of the unannealed aggregates, but there is still a large spread in lifetimes. Again, it is likely that the concentration of quenching defects varies widely in the unannealed aggregates, which leads to different quenching rates and different fluorescence lifetimes. Solvent annealing allows the aggregates to reassemble into something closer to their equilibrium structures, resulting in the more regular surfaces and edges seen in the AFM images. The spectral behavior becomes much more uniform, and the variation in relaxation times, although still present, is much less pronounced. However, even the annealed aggregates are clearly not defect-free crystals. The fluorescence spectrum continues to shift and change shape even at the lowest temperatures, providing evidence for multiple energy sites within a single aggregate. Relaxation to these sites must be an activated process, however, since at low temperatures the amount of shifting and shape changing is greatly decreased.

It might be surprising aspects that we see any variation at all between the aggregates. Each aggregate contains roughly 10^7 – 10^8 DSB molecules, and it is not obvious why such a large ensemble should not average over every possible configuration and appear bulklike. It may be that organic aggregates are subject to a size effect, in that limiting the size limits the ability of the aggregate to include all possible defects, and thus its ability to mimic the bulk. One way to interpret these results is to picture the initially excited state, most likely an exciton in a locally ordered region of the aggregate, undergoing diffusion on a random energy landscape³⁸ whose structure and statistics depend sensitively on the preparation conditions. Different aggregates have different landscapes. This concept may help explain why the spectrum of the annealed aggregates still

undergoes measurable changes even at 4 K, whereas the spectrum of the unannealed aggregates is constant at that temperature, with only a slight redshift. If the energy landscape of an unannealed aggregates is "rougher" due to its rapid formation, it would then be easier for an exciton to remain trapped on its locally ordered site at low temperature, as opposed to having a high density of energetically similar sites nearby in a less corrugated landscape, as would be the case in the annealed aggregates.

Given all of the variations observed in the aggregate spectra, it is an open question as to whether it is possible to extract the intrinsic exciton spectrum of crystalline DSB from experiments on such samples. Despite the spectral variations observed at 290 K, all of the aggregates studied in this work exhibit similar spectra at 4 K, which suggests that they possess a common emitting species despite significant differences in preparation conditions and morphology. This spectrum is seen most clearly in the annealed aggregates at 4 K at early times, where the 0–0 peak is most pronounced and blue shifted, and the 0–1 peak is the largest relative to the 0–2 and 0–3 peaks. However, even this spectrum probably contains some contribution from the redshifted defect species, and it still evolves over the course of nanoseconds. Our analysis of the 100 K annealed spectrum illustrates the assumptions involved in decomposing a multi-component decay into pure, single component spectra. It is likely that the spectrum obtained from our fitting is the closest to the intrinsic exciton in the DSB crystal, and it certainly would be the one to compare with theoretical calculations in order to estimate an exciton coherence length for the material. Although the emission spectra of the different excited-state species overlap, it may be that their transient absorption spectra are well-separated. In this case, pump–probe spectroscopy on the individual aggregates, although technically difficult, might be an even more informative experiment.³⁹

In conclusion, we have used AFM and picosecond time-resolved fluorescence microscopy to examine the temperature-dependent dynamics of individual DSB aggregates. We find systematic differences between annealed and unannealed aggregates and also differences between aggregates within the same sample. The variations in relaxation times and spectral evolution are more pronounced in the unannealed samples, which have widely varying relaxation times even at 4 K. Using a multiple wavelength biexponential fitting procedure, we can extract the spectra of the different emitting species, with the higher energy species likely corresponding to the intrinsic exciton of the DSB crystal. An interesting result of our work is that even relatively large aggregates, on the order of hundreds of nanometers, still exhibit considerable variation in the relative amount of the two excited-state species we have identified. Our analysis shows that it is possible to overcome the sample dependence in the optical spectroscopy of organic aggregates and that a combination of microscopy and careful spectroscopic analysis may serve as a useful complement to the study of macroscopic, defect-free single crystals, which is a challenging task in its own right.

Acknowledgment. We acknowledge support from the NSF (CHE-99-84683), the ACS Petroleum Research Fund (36463-G7), and a 3M Untenured Faculty Award. C.J.B. is an Alfred P. Sloan Research Fellow.

References and Notes

- (1) Friend, R. H.; Gymer, R. W.; Holmes, A. B.; Burroughes, J. H.; Marks, R. N.; Taliani, C.; Bradley, D. D. C.; Santos, D. A. D.; Bredas, J. L.; Logdlund, M.; Salaneck, W. R. *Nature* **1999**, *397*, 121–128.
- (2) Heeger, A. J. *J. Phys. Chem. B* **2001**, *105*, 8475–8491.
- (3) Hutten, P. F. v.; Krasnikov, V. V.; Hadzioannou, G. *Acc. Chem. Res.* **1999**, *32*, 257–265.
- (4) Mullen, K.; Wegner, G. *Adv. Mater.* **1998**, *10*, 433–436.
- (5) Egelhaaf, H.-J.; Gierschner, J.; Oelkrug, D. *Synth. Met.* **1996**, *83*, 221–226.
- (6) Gierschner, J.; Egelhaaf, H.-J.; Oelkrug, D. *Synth. Met.* **1997**, *84*, 529–530.
- (7) Oelkrug, D.; Tompert, A.; Egelhaaf, H.-J.; Hanack, M.; Steinhuber, E.; Hohloch, M.; Meier, H.; Stalmach, U. *Synth. Met.* **1996**, *83*, 231–237.
- (8) Oelkrug, D.; Tompert, A.; Gierschner, J.; Egelhaaf, H.-J.; Hanack, M.; Hohloch, M.; Steinhuber, E. *J. Phys. Chem. B* **1998**, *102*, 1902–1907.
- (9) Spano, F. C.; Siddiqui, S. *Chem. Phys. Lett.* **1999**, *314*, 481–487.
- (10) Spano, F. C. *J. Chem. Phys.* **2001**, *114*, 5376–5390.
- (11) Spano, F. C. *J. Chem. Phys.* **2002**, *116*, 5877–5891.
- (12) Spano, F. C. *J. Chem. Phys.* **2003**, *118*, 981–994.
- (13) Ni, J. P.; Ueda, Y.; Hanada, T.; Takada, N.; Ichino, Y.; Yoshida, Y.; Tanigaki, N.; Yase, K.; Wang, D. K.; Wang, F. S. *J. Appl. Phys.* **1999**, *86*, 6150–6154.
- (14) Ni, J. P.; Ueda, Y.; Ichino, Y.; Yase, K.; Wang, D. K. *Thin Solid Films* **2000**, *363*, 86–89.
- (15) Summers, M. A.; Robinson, M. R.; Bazan, G. C.; Buratto, S. K. *Synth. Met.* **2003**, *137*, 957–958.
- (16) Veenstra, S. C.; Hutten, P. F. v.; Post, A.; Wang, Y.; Hadzioannou, G.; Jonkman, H. T. *Thin Solid Films* **2002**, *422*, 104–111.
- (17) Higgins, D. A.; Barbara, P. F. *J. Phys. Chem.* **1995**, *99*, 3–7.
- (18) Reid, P. J.; Higgins, D. A.; Barbara, P. F. *J. Phys. Chem.* **1996**, *100*, 3892–3899.
- (19) Hofkens, J.; Latterini, L.; Vanoppen, P.; Faes, H.; Jeuris, K.; Feyter, S. D.; Kerimo, J.; Barbara, P. F.; Schryver, F. C. D.; Rowan, A. E.; Nolte, R. J. M. *J. Phys. Chem. B* **1997**, *101*, 10588–10598.
- (20) Bout, D. A. V.; Kerimo, J.; Higgins, D. A.; Barbara, P. F. *Acc. Chem. Res.* **1997**, *30*, 204–212.
- (21) Kook, S.-K.; Kopelman, R. J. *J. Phys. Chem.* **1992**, *96*, 10672–10676.
- (22) Birnbaum, D.; Kook, S.-K.; Kopelman, R. J. *J. Phys. Chem.* **1993**, *97*, 3091–3094.
- (23) Yoshikawa, H.; Sasaki, K.; Masuhara, H. *J. Phys. Chem. B* **2000**, *104*, 3429–3437.
- (24) Yoshikawa, H.; Masuhara, H. *J. Photochem. Photobiol. C* **2000**, *1*, 57–78.
- (25) Henke, L.; Nagy, N.; Krull, U. J. *Biosens. Bioelectron.* **2002**, *17*, 547–555.
- (26) Karabunarliev, S.; Baumgarten, M.; Bittner, E. R.; Mullen, K. J. *Chem. Phys.* **2000**, *113*, 11372–11381.
- (27) Gierschner, J.; Mack, H.-G.; Luer, L.; Oelkrug, D. *J. Chem. Phys.* **2002**, *116*, 8596–8609.
- (28) Kasha, M.; Rawls, H. R.; El-Bayoumi, M. A. *Pure Appl. Chem.* **1965**, *11*, 371–392.
- (29) Bjorklund, T. G.; Lim, S.-H.; Bardeen, C. J. *Synth. Met.* **2002**, *126*, 295–299.
- (30) Nguyen, T.; Martini, I. B.; Liu, J.; Schwartz, B. J. *J. Phys. Chem. B* **2000**, *104*, 237–255.
- (31) Shi, Y.; Liu, J.; Yang, Y. *J. Appl. Phys.* **2000**, *87*, 4254–4263.
- (32) Rep, D. B. A.; roelfsema, R.; Esch, J. H. v.; Schoonbeek, F. S.; Kellogg, R. M.; Feringa, B. L.; Palstra, T. T. M.; Klapwijk, T. M. *Adv. Mater.* **2000**, *12*, 563–566.
- (33) Thalladi, V. R.; Whitesides, G. M. *J. Am. Chem. Soc.* **2002**, *124*, 3520–3521.
- (34) Birks, J. B. *Photophysics of aromatic molecules*; Spottiswoode, Ballantyne & Co.: London, 1970.
- (35) Bout, D. A. V.; Kerimo, J.; Higgins, D. A.; Barbara, P. F. *J. Phys. Chem.* **1996**, *100*, 11843–11849.
- (36) Meskers, S. C. J.; Janssen, R. A. J.; Haverkort, J. E. M.; Wolter, J. H. *Chem. Phys.* **2000**, *260*, 415–439.
- (37) McQuade, D. T.; Kim, J.; Swager, T. M. *J. Am. Chem. Soc.* **2000**, *122*, 5885–5886.
- (38) Wang, J.; Saven, J. G.; Wolynes, P. G. *J. Chem. Phys.* **1996**, *105*, 11276–11284.
- (39) Tamai, N.; Porter, C. F.; Masuhara, H. *Chem. Phys. Lett.* **1993**, *211*, 364–370.